Edge-Controlled Growth and Etching of Two-Dimensional GaSe Monolayers

Xufan Li,[†] Jichen Dong,[‡] Juan C. Idrobo,[†] Alexander A. Puretzky,[†] Christopher M. Rouleau,[†] David B. Geohegan,[†] Feng Ding,*[‡,§] and Kai Xiao*[†]

[†]Center for Nanophase Materials Sciences, Oak Ridge National Laboratory, Oak Ridge, Tennessee 37831, United States
[‡]Center for Multidimensional Carbon Materials (CMCM), Institute for Basic Science (IBS), Ulsan 689-798, Republic of Korea
[§]School of Materials Science and Engineering, Ulsan National Institute of Science and Technology (UNIST), Ulsan 689-798, Republic of Korea

S *Supporting Information*

ABSTRACT: Understanding the atomistic mechanisms governing the growth of two-dimensional (2D) materials is of great importance in guiding the synthesis of wafer-sized, single-crystalline, high-quality 2D crystals and heterostructures. Etching, in many cases regarded as the reverse process of material growth, has been used to study the growth kinetics of graphene. In this work, we explore a growth–etching–regrowth process of monolayer GaSe crystals, including single-crystalline triangles and irregularly shaped domains formed by merged triangles. We show that the etching begins at a slow rate, creating triangular, truncated triangular, or hexagonally shaped holes that eventually evolve to exclusively triangles that are rotated 60° with respect to the crystalline orientation of the monolayer triangular crystals. The regrowth occurs much faster than etching, reversibly filling the etched holes and then enlarging the size of the monolayer crystals. A theoretical model developed based on kinetic Wulff construction (KWC) theory and density functional theory (DFT)

calculations accurately describe the observed morphology evolution of the monolayer GaSe crystals and etched holes during the growth and etching processes, showing that they are governed by the probability of atom attachment/detachment to/from different types of edges with different formation energies of nucleus/dents mediated by chemical potential difference $\Delta\mu$ between Ga and Se. Our growth–etching–regrowth study provides not only guidance to understand the growth mechanisms of 2D binary crystals but also a potential method for the synthesis of large, shape-controllable, high-quality single-crystalline 2D crystals and their lateral heterostructures.
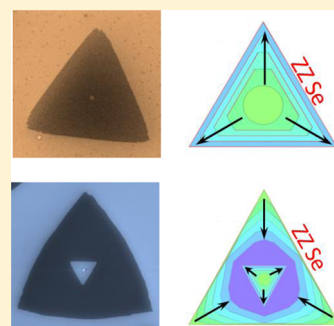
INTRODUCTION

Two-dimensional (2D) crystals including graphene, hexagonal boron nitride (h-BN), transition metal dichalcogenides (i.e., TMX$_2$, TM = Mo, W; X = S, Se, and Te), and metal monochalcogenides (i.e., MX, M = Ga, In; X = S, Se, and Te) have attracted tremendous interest because of their unique optical and electrical properties, and great potential for applications in next-generation optoelectronic devices.[1−4] The most significant challenge to realize applications for these materials is the scalable synthesis of large-area (i.e., wafer-sized) and high-quality 2D single crystals.[5,6] Chemical vapor deposition (CVD) is the most versatile and promising method to synthesize large (from micrometer to inch size) monolayer domains of graphene, h-BN, TMX$_2$, and MX[7−11] crystals. However, for demanding electronic applications, the quality of most CVD-grown 2D crystals still needs to be improved (e.g., the carrier mobility of CVD-grown 2D crystals is generally lower than their mechanically exfoliated counterparts).[12,13] This is likely due to defects incorporated during growth; therefore, understanding atomistic growth and etching mechanisms is both fundamentally important and crucial for controlling and

optimizing not only the size and morphology of 2D crystals, but also their quality.

Commonly, the growth of thin films on various types of substrates is explained by one or more of the following mechanisms: Volmer−Weber (VW, formation of three-dimensional adatom clusters or islands), Frank−van der Merwe (FM, also called layer-by-layer growth), and Stranski−Krastanov (SK, also called layer-plus-island growth). These also can be generally applied to the CVD growth of 2D crystals.[14,15] In particular, the formation of large and well-separated, single-crystalline 2D monolayer domains, as well as continuous monolayer or few-layer 2D films are very likely to follow FM growth.[7,8,11] In addition, the nucleation of 2D crystals grown on different types of substrates always shows that the nucleation density is controlled by defects or grain boundaries on the substrate[16−18] or by gas-phase species supplied through the carrier gas flow.[19] Understanding nucleation and growth modes of 2D crystals is essential to guide strategies for controllable and optimized synthesis. However, the above-mentioned three

growth modes are unable to explain the growth kinetics governing the morphological evolution of the 2D domains, their edge structures, or the formation of grain boundaries by coalescence of single-crystalline domains.

Etching and growth are complementary processes, involving the removal and addition of building blocks to a material. The two processes compete during 2D crystal synthesis. Therefore, understanding the etching process can shed light on the growth mechanism by revealing the details of the addition or removal of atoms. Recently, the growth and etching of graphene and h-BN into different shapes have been demonstrated, indicating that the growth of graphene and h-BN is controlled by the competition between attachment kinetics and adatom diffusion.[20−22] Recent studies revealed that the growth and etching of graphene are two reversible processes, or in other words, faster-growing edges during material growth correspond to faster-etching edges during etching.[23−26] This results from atomistic arguments that both growth and etching rates are strongly dependent on the edge structure.[23−26] For example, the morphology evolution of graphene in the growth, etching, and regrowth processes have been theoretically explained using classical kinetic Wulff construction (KWC) theory and its modifications.[26] A full understanding of the atomistic and thermodynamic arguments reflected in the growth kinetics is required to develop a strategy for the fabrication of large-area, defect-free, single-crystalline graphene[6,26] and other 2D crystals through repeated growth-etching-regrowth processes.

Compared with graphene, 2D crystals with binary compositions (i.e., h-BN, TMX_2, and MX) not only show richer edge structures due to the binary components in the crystal lattice and the lower lattice symmetry,[27,28] but also involve more complicated growth processes because of the number of possibilities introduced by different atom-by-atom accretion sequences. In addition, TMX_2 and MX can be grown directly on a much richer variety of substrates compared with graphene and h-BN as the growth of TMX_2 and MX normally does not require a metal catalyst. Thus, investigating the growth and etching process of TMX_2 or MX monolayers will provide valuable and broader insights into the growth kinetics of 2D crystals.

GaSe is an important layered material, and 2D GaSe atomic layers have attracted much attention due to their unique optoelectronic,[11,29−31] nonlinear optical,[32] as well as theoretically predicted magnetic properties.[33] The synthesis of large-sized, single-crystalline GaSe monolayers on different substrates including SiO_2/Si,[11] graphene,[16] and $MoSe_2$ monolayers[34] has been demonstrated by our group, using a vapor-phase deposition method involving the vaporization of bulk GaSe crystals. However, due to a high growth rate, it is difficult to investigate the detailed edge and shape evolution of GaSe monolayers in the initial growth stage, which presents a challenge to understand the growth mechanisms.

In this work, we develop a growth−etching−regrowth process to understand the growth kinetics and edge stabilities of GaSe monolayers during the vapor-phase deposition process by tuning the carrier gas (argon) flow. Switching from growth to etching formed holes with hexagonal, truncated triangular, and triangular morphologies in the single crystal domains, and a variety of different morphologies near the grain boundaries. Experimental observation and theoretical simulation showed that the morphology evolution of the monolayer GaSe crystals and etched holes during the growth and etching processes followed KWC theory and was edge-structure-dependent,

which is governed by the probability of atom attachment/detachment to/from different types of edges with different formation energies of nuclei/dents mediated by the chemical potential difference $\Delta\mu$ between Ga and Se.

■ RESULTS AND DISCUSSION

2D GaSe crystals were grown on SiO_2/Si substrates through a vapor-phase deposition method, in which bulk GaSe crystals are vaporized at 750 °C, and the vapor was carried by an Ar gas flow to feed the growth of the 2D GaSe crystals (see Experimental Section for the detailed synthesis method).[11] Figure 1a shows an optical micrograph of GaSe monolayers, in
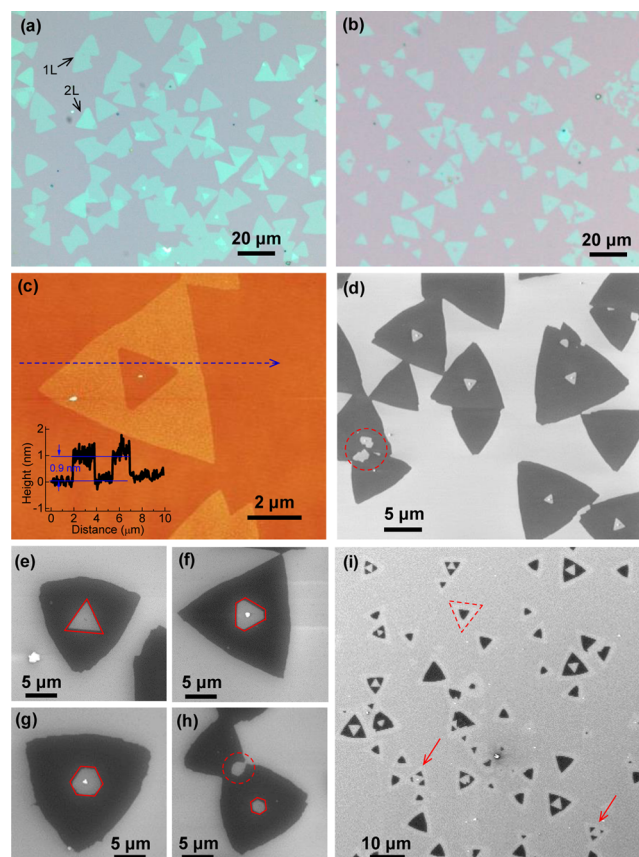
Figure 1. Morphologies of as-grown and etched GaSe monolayers. (a) Optical micrograph of 2D GaSe crystals grown for 3 min. (b) Optical micrograph GaSe monolayers after being etched for 3 min. (c) AFM image of a triangular GaSe monolayer after being etched 5 min. Inset is the height profile along the dashed blue line. (d−h) SEM images of GaSe monolayers after being etched for 5 min, showing different shapes of the etched holes. (i) SEM image of GaSe monolayers after being etched for 20 min. The etching process started after growth for 3 min.

which small patches of bilayer domains are also observed. The crystal thickness is confirmed by atomic force microscope (AFM) analyses (Figures S1 and 1c). The GaSe monolayers are generally triangular in shape (with some showing minor truncated vertices), containing both separated triangles and domains formed by the merging of individual triangles with different orientations. As shown in our previous report,[11] the triangular-shaped monolayers are single-crystalline GaSe with a hexagonal crystal structure. The grain boundaries are formed in the domains of merged individual triangles with different orientations.
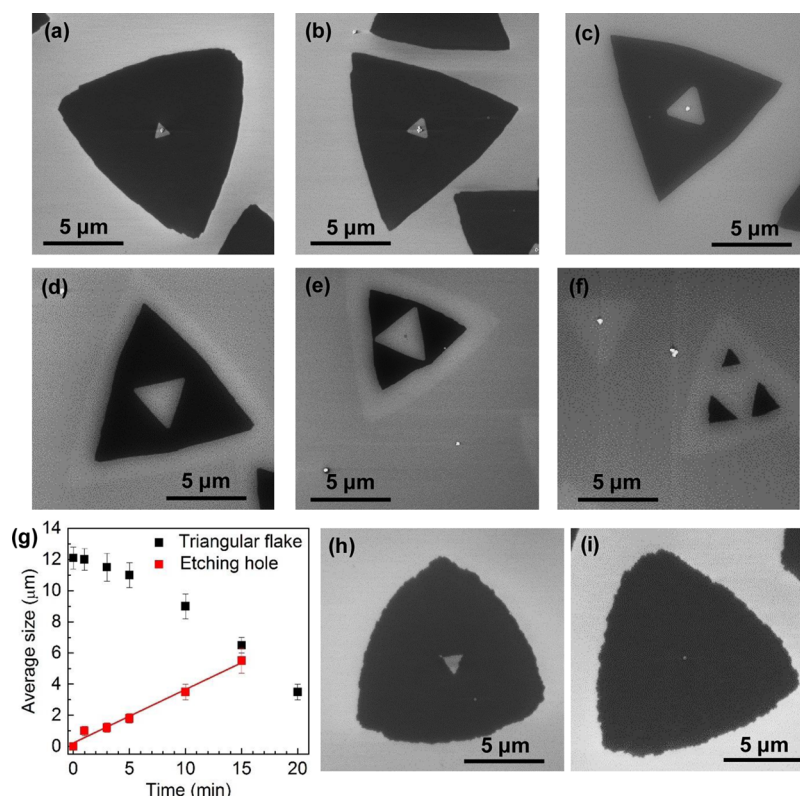
Figure 2. Etching rate of GaSe monolayers. (a−f) SEM images of typical triangular GaSe monolayers after being etched for (a) 1 min, (b) 3 min, (c) 5 min, (d) 10 min, (e) 15 min, and (f) 20 min. The etching process started after 3 min growth. The low magnification SEM images for each etching time are shown in Figure S4. (g) Evolution of the size of triangular GaSe monolayers (black squares) and etched holes (red squares) as a function of etching time. The statistics were performed on low-magnification SEM images shown in Figure S4. (h−i) SEM images of regrown GaSe monolayers by resuming argon carrier gas flow for 1 and 2 min, respectively, after being etched for 15 min.

However, when the argon carrier gas flow was cut off during the growth process and the furnace temperature was rapidly increased from 750 to 760 °C, growth switched to etching. Holes appeared in some GaSe monolayers, which were observable under an optical microscope (Figure 1b) and AFM (Figure 1c). Both the AFM image (Figure 1c) and scanning electron microscope (SEM) images (Figure 1d,e) reveal that most holes are triangular in shape as are the parent domains, but the triangular holes are rotated by 60° relative to the parent domains. Further observations using SEM indicate that the etched holes on GaSe monolayers are not exclusively triangular in shape. Actually, at the early stage of etching (e.g., for etching lasting less than 5 min), truncated triangular (Figure 1f) or hexagonal holes (Figure 1g,h) are also formed. However, as the etching process continues, the shapes of the holes eventually evolve exclusively into triangles (Figure 1i). As a triangular hole reaches the edges of a triangular domain, it separates a single triangular domain into three smaller triangular domains as indicated by the red arrows in Figure 1i, and continuous etching was observed to gradually shrink the three smaller domains until their disppearance. Also in Figure 1i, a triangular contour can be observed outside every etched monolayer (as highlighted by a dashed red triangle) that corresponds to the original size and the shape of each single crystalline domain before etching. Such visible contrast differences in the secondary electron yield between the etched regions and the regions where no GaSe crystals grew are likely indications of different chemical states between the two regions. Although it is currently unclear what causes the contrast

difference, a possible reason could be chemical interactions with the substrate such as Ga−Si bonding, as was observed in a previous report.[35] The SEM results indicate that although etching does not create holes for every GaSe single crystalline domain every crystal is etched from their edges.

From the SEM images, the etched holes are observed to originate at the locations of small Ga, Se, or GaSe particles (as proven by energy-dispersive X-ray spectroscopy in the SEM) (Figures 1d,f,g and S2a,b). These particles were formed during the growth and are generally located at the center of a 2D crystal but can occasionally be observed at other locations. Besides particles, etched holes are also formed at the center of GaSe monolayers that did not contain these particles (Figures 1e,h and S2a) and at the grain boundaries between merged triangular crystals (as indicated by dashed red circles in Figure 1d,h; see Figure S2c as well). Note that in the region close to the upstream side of the substrate an apparently continuous GaSe monolayer film (with some multilayer crystals on top) is formed by merging randomly oriented individual GaSe monolayer crystals with multiple grain boundaries (Figure S3a).[11] After etching, such continuous monolayer films show many irregularly shaped holes originating at the grain boundaries (Figure S3b,c). The fact that the etching prefers to originate at the edges and center of the triangular monolayers, at deposited particles, and at grain boundaries indicates that those positions are energetically favorable for the detachment of Ga and Se atoms. Compared to monolayers, comparable etching is much harder to achieve for bilayers and thicker crystals (Figure S2d−f). Moreover, etched holes were
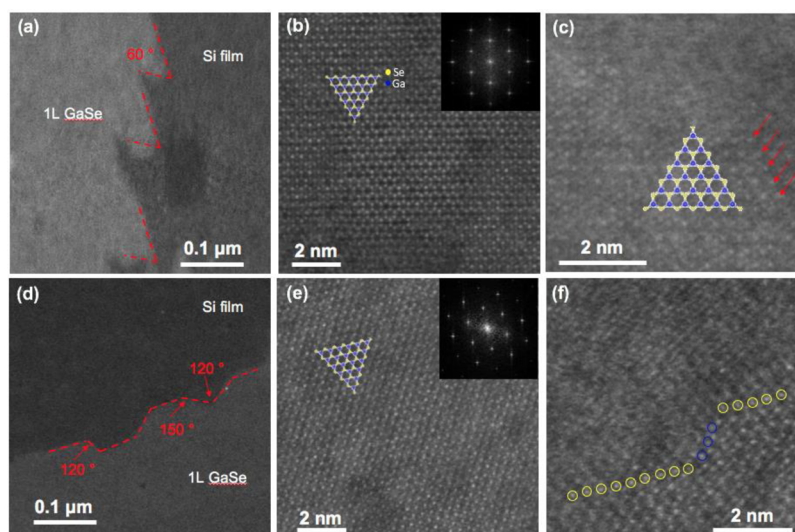
Figure 3. Structures of as-grown and etched GaSe monolayers. (a) Low-magnification ADF-STEM image showing the edge area of an as-grown triangular GaSe monolayer (without etching). (b−c) Atomic-resolution ADF-STEM images showing the atomic structure of GaSe monolayer in the inner region (b) and close to the edge (c). Atomic models of monolayer GaSe are overlaid. Inset of (b) is the corresponding fast Fourier transform (FFT) pattern. The red arrows in (c) indicate the visible atoms (Se) closest to the edge. (d) Low-magnification ADF-STEM image showing the edge area of a triangular GaSe monolayer after being etched for 5 min. (e−f) Atomic-resolution ADF-STEM images showing the atomic structure of the etched GaSe monolayer in the inner region (e) and close to the edge (f). Atomic model of monolayer GaSe is overlaid. Inset of (e) is the corresponding FFT pattern. The circles in (f) indicate the visible atoms (yellow for Se, blue for Ga) closest to the edge.

never observed inside the bilayer crystals, but only at their vertices (Figure S2e,f). This will be discussed later.

To get a quantitative understanding of the etching process, the size evolution of both GaSe monolayers and etched holes were measured as a function of etching time for different growth experiments. To ensure that the etching time is the only variable in the comparative experiments, the etching process was started after 3 min of growth in each case and observed for the same growth region on the downstream side of the substrate for each etching time. Figure 2a−f shows typical triangular GaSe monolayers after being etched for 1, 3, 5, 10, 15, and 20 min, respectively. Due to the inhomogeneity of the crystal size before etching, a statistical analysis was performed on low-magnification SEM images with a large number of crystals (Figure S4). The average lateral sizes of the crystals and etched holes versus etching times are plotted in Figure 2g. The reduction of lateral length of the triangular GaSe monolayers during etching generally exhibits nonlinear behavior as a function of time. A similar monolayer domain etching behavior was observed in the etching of graphene, which was believed to be edge-structure-dependent where fast-etching edges gradually develop during the process.[26] During the etching process, the fastest etching edges are at 19° with respect to the zigzag edges, and first appearing at the vertices of the triangular GaSe flake and then extending to the flake circumference. Therefore, a nonlinear reduction of the triangle's lateral length appears during the etching process. On the contrary, the expansion of the etched holes is nearly linear (Figure 2g), indicating no change of the edge type along each edge of the triangular etched holes.

The etching process can be switched back to growth (regrowth) by resuming the argon gas flow after cooling the temperature back down to 750 °C (Figure 2h,i). The vaporized reactant species attach seamlessly to both outer and inner edges of the etched monolayers (Figure S5), resulting in increasing crystal size and filling of the etched holes. However, the

regrowth rate is observed to be much faster than the etching rate. After regrowth for only 2 min, all the etched holes are totally refilled, and the crystal has almost enlarged to return to the original size (Figure 2i). However, the regrown GaSe monolayers edges are more curved and have rougher edges than the crystals grown originally. These may be caused by additional nucleation sites along the edges resulting from clusters generated by the transient reaction chamber pressure when the argon gas flow is resumed. Understanding this difference in GaSe crystal shape and quality requires more detailed studies and control of the regrowth process, which will be the subject of our future work.

In order to get a deeper insight into the growth and etching behavior of the GaSe monolayers, edge structures of monolayer GaSe crystals were investigated using annular dark-field (ADF) imaging in an aberration-corrected scanning transmission electron microscope (STEM). Figure 3a shows an ADF-STEM image highlighting the edge morphology of an as-grown triangular GaSe monolayer without etching. Although the edge is not straight, it is sawtooth shaped with each angle at generally 60° (which is also observed in our previous work).[11] It indicates that the structure along this edge is coherent, which could be either zigzag (Ga- or Se-terminated) or armchair. Figure 3b shows the honeycomb atomic structure of monolayer GaSe along [001] direction with the in-plane distance between two adjacent Ga (or Se) of ∼0.38 nm, in agreement with our previous report.[11] However, the edge of the monolayer is much more vulnerable than the inner region, resulting in quick damage to the lattice by the electron beam (Figure 3c). Although it is hard to distinguish the atomic structure at the edge due to the electron beam damage, from the analysis of the atomic structure close to the edge (as indicated by the red arrows in Figure 3c), we conclude that the observed edge structure of this GaSe monolayer is zigzag. The edge morphology of the etched GaSe monolayer is also shown in the low magnification ADF-STEM image (Figure 3d).

Interestingly, after etching, the sawtooth shaped edge of the monolayer turns from uniform 60° angles to a variety of angles containing 120 and 150°, suggesting that the coherent edge structure evolved into a combination of different types of edge structures. The atomic-resolution ADF-STEM image indicates that the overall crystal structure of the GaSe monolayers is not damaged or altered after etching (Figure 3e), indicating that the etching is a steady process controlled by the kinetics of atoms removal at the edges. Similar to the as-grown GaSe monolayers, the edge of the etched monolayers also undergoes quick damage under the electron beam (Figure 3f). The atoms close to the edge show a twisted arrangement at 120°, featuring an edge with both Se- and Ga-terminated zigzag (as indicated by yellow and blue circles in Figure 3f).

To explain the experimentally observed shape evolution of GaSe monolayer domains and etched holes, as well as to understand the atomistic growth and etching mechanisms, we theoretically modeled the morphologies of flakes and etched holes, which could be determined by either energies of the edges at equilibrium or by nonequilibrium growth kinetics at the edges. We first consider the equilibrium shape of monolayer GaSe domains. For GaSe with the hexagonal crystal structure, the 3-fold symmetry leads to the following types of edges: Ga-terminated zigzag (called Ga-zigzag hereafter), Se-terminated zigzag (called Se-zigzag hereafter), armchair (Figure 4a), and
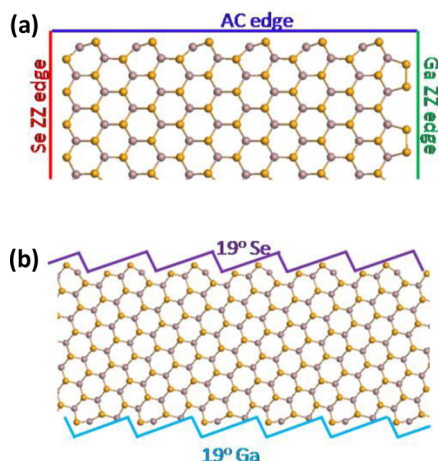

Figure 4. Different edge structures of hexagonal GaSe. (a) Ga-zigzag, Se-zigzag, and armchair edges. (b) Tilted edges between zigzag and armchair configurations with a tilt angle of about 19° with respect to zigzag edges.

tilted between zigzag and armchair configurations (Figure 4b). We found that armchair and Se-zigzag edges are stable while the Ga atoms at the Ga-zigzag edge are likely to be passivated by Se (as shown in Figure 4a and Figure S6). A bare Ga-zigzag edge is severely distorted after structure optimization, suggesting its instability (Figure S6c). This result is similar to the case of MoS$_2$, for which Mo terminated zigzag edges require passivation by S (refs36 and 37). The formation energies of these edges were calculated (see the Experimental Section for detailed calculation methods). Unlike graphene, the edge energy of GaSe depends on the chemical potential difference between Ga and Se atoms, $\Delta\mu$. Due to the unbalanced stoichiometry between Ga and Se for zigzag edges, the formation energies of the Ga- and Se-zigzag edges show a linear dependence on $\Delta\mu$ (Figure S7a). With this result, the

formation energies of any other tilted edges can be estimated by a cosinoidal function of the tilt angle, θ (Figure S7b).[23] Therefore, the equilibrium shape of monolayer GaSe flakes can be obtained by traditional (thermodynamic) Wulff construction. As a result, with the increase of $\Delta\mu$, equilibrium GaSe flakes are predicted to show truncated triangular shapes with the long and short edges being Se- and Ga-zigzag edges, nonagonal shapes enclosed by Se-zigzag and armchair edges, and hexagonal shapes with armchair edges (Figure S7c). Although we do observe some truncated triangular monolayer domains, the majority of the as-grown flakes have triangular shapes, which is not predicted by the equilibrium edge energy calculation. Therefore, below we consider the growth and etching kinetics at the edges.

The growth/etching kinetics of GaSe flakes is mediated by the probability of atom attachment/detachment to/from zigzag, armchair, and tilted edges, as inferred from Ma's study on the edge controlled synthesis of graphene.[26] During growth, edges with very fast growth rates disappear and the morphology of the grown structures is determined by slow-growing edges, which is a simple consequence of KWC theory. On tilted edges, there are kinks with a concentration approximately proportional to the tilt angle (θ) that can serve as easy attachment/detachment points for atoms. The attachment to these kinks requires almost negligible extra energy. However, the growth/etching of both zigzag and armchair edges needs to be initiated by the formation of a nucleus/dent at a relatively large energy cost. Therefore, the growth morphology of hexagonal GaSe should be governed by the slow-growing edges, while the etching morphology is determined by the fast-etched tilted edges. According to previous reports, tilted edges with a tilt angle θ of ~19.1° with respect to zigzag edges have the largest kink density.[23,24] Therefore, such edges exhibit maximum growth/etching rate locally. For GaSe, there are two kinds of such edges, which are close to Se-zigzag and Ga-zigzag edges, respectively. Hereafter, we refer to these two types of tilt edges as 19° Se and 19° Ga edges (Figure 4b).

According to previous studies, the growth/etching rate of the edge is determined by the formation energies (E_F) of kink nuclei/dents on the zigzag and armchair edges.[24,26,38] The equation to estimate the growth/etching rate of an edge with an arbitrary tilt angle with respect to the zigzag edge is described in the Experimental Section, which indicates that the higher the formation energy, the slower the growth rate of the edge. Therefore, in order to calculate the growth rate of different edges, we need to first obtain their formation energy profiles. To this end, the step flow growth model is employed, and the formation energies of step-by-step attachment of atoms to the edges are calculated, as shown in Figure S8. It can be seen that the growth of the armchair and zigzag edge is initiated by the attachment of Ga and Se atoms to form a kink site, and then dictated by consecutive addition of Ga and Se atoms at kinks (Figure S8). Figure 5a shows the formation energy profile of the step flow growth processes of zigzag and armchair edges at $\Delta\mu = 0$ eV. We define the formation energy E^*_F for initiating the growth of a certain type of edge as the highest energy cost for each step in the growth process. Thus, the E^*_F for armchair edge is 1.19 eV (i.e., with the addition of 6 and 8 pairs of Ga and Se atoms as shown in Figure S8a), 1.45 eV for Ga-zigzag edge growth (with the addition of 6 pairs of Ga and Se atoms at the edge), and 1.75 eV for Se-zigzag edge growth (with the addition of 4 Ga and 2 Se atoms). The above results indicate that at $\Delta\mu = 0$ eV, the Se-zigzag edge and armchair edge show
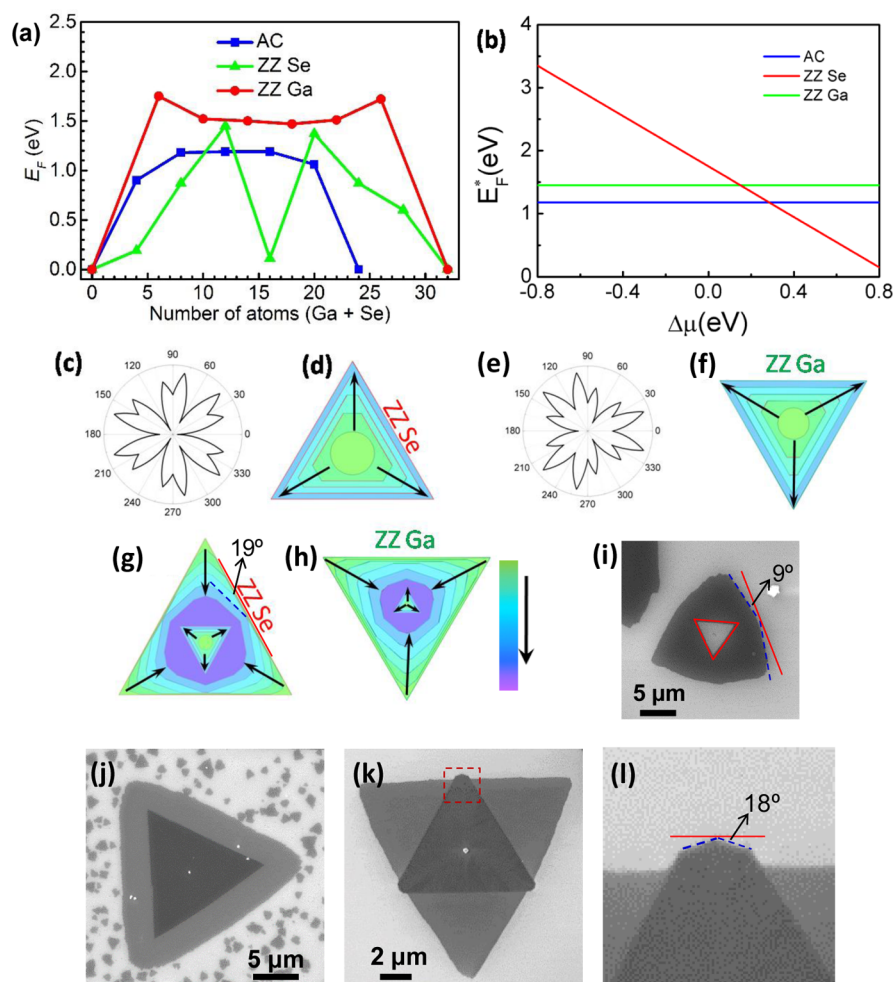
Figure 5. Calculations of growth and etching kinetics. (a) Formation energy change profile of the growth process of different edges at $\Delta\mu$ = 0 eV. (b) Change of the formation energy costs for initiating the growth of zigzag and armchair edges as a function of $\Delta\mu$. (c) Polar plot of growth/etching rate at $\Delta\mu$ = 0.06 eV. (d) Simulated growth of GaSe from a circular nucleus $\Delta\mu$ = 0.06 eV. (e) Polar plot of growth/etching rate at $\Delta\mu$ = 0.24 eV. (f) Simulated growth of GaSe from a circular nucleus $\Delta\mu$ = 0.24 eV. (g, h) Simulated etching process of as-grown GaSe domains at $\Delta\mu$ = 0.06 and 0.24 eV, respectively. The arrows in (d) and (f–h) show the shape evolution directions. The shadowed areas with different colors in (d) and (f–h) show different growth/etching stages, as shown by the color bar. (i) SEM image of a typical etched GaSe monolayer polygon on SiO_2/Si substrate, showing tilt edges with a tilt angle about 9° with respect to the zigzag Se (Ga) edge. (j) SEM image of an as-grown bilayer GaSe flake showing sharp vertices of the second layer. (k) SEM image of a bilayer GaSe flake at the initial etching stage. (l) Enlarged view of the region contained by dashed square in (k).

the highest (1.75 eV) and lowest (1.19 eV) free energy barrier, respectively, for kink formation; therefore, the growth rate sequence of the three types of edges is armchair > Ga-zigzag > Se-zigzag at $\Delta\mu$ = 0 eV. It is worth noting that the growth of armchair and Ga-zigzag is mediated by attaching pairs of Ga and Se atoms (i.e., with balanced stoichiometry between Ga and Se) to the edge, while the attachment of atoms to the Se-zigzag edge is unbalanced in stoichiometry (Figure S8). Therefore, the E^*_F for initiating the growth of the armchair and Ga-zigzag edges are constant as a function of $\Delta\mu$, while E^*_F decreases as $\Delta\mu$ increases for Se-zigzag edge (Figure 5b). At $\Delta\mu$ = 0.15 eV, E^*_F for the Se-zigzag edge becomes equal to that for the Ga-zigzag edge, implying equal growth rates between these two zigzag edges. As $\Delta\mu$ becomes larger than 0.15 eV, the Se-zigzag edge grows faster than Ga-zigzag edge, and it grows at the same rate as the armchair edge when $\Delta\mu$ further increases to 0.28 eV (Figure 5b). The change of the relative growth rates between zigzag and armchair edges induced by $\Delta\mu$ suggests that the experimentally grown GaSe flakes can show various

shapes enclosed by zigzag or armchair edges, depending on growth conditions.

To further verify this, we calculated the shape evolution of monolayer GaSe flakes during growth using the KWC theory with the growth rate profiles estimated (using eq 1 described in the Experimental Section) at different $\Delta\mu$ at a temperature of 700 °C. Figure 5c and 5e show the polar plots of estimated growth rate profiles at $\Delta\mu$ = 0.06 and 0.24 eV, respectively (see Figure S9 for the growth rate profiles at other $\Delta\mu$ values). Here, the Se-zigzag edge is chosen as the reference (at 0°) for the polar plots. As a consequence of the high symmetry structures, the growth rates of zigzag and armchair edges correspond to local minima in the plot (i.e., at 0, 120, and 240° for the zigzag Se edge, at 60, 180, and 300° for the zigzag Ga edge, and at 30, 90, 150, 210, 270, and 330° for the armchair edge). As shown in Figure 5b, the Se-zigzag edge grows at a slower rate than that of the Ga-zigzag edge at $\Delta\mu$ = 0.06 eV, while the sequence is reversed at $\Delta\mu$ = 0.24 eV. The armchair edge always grows faster than both zigzag edges because of its lower formation

energy. In contrast, the two 19° edges grow faster than all the other edges because of their highly kinked structures (Figure 4b) and the consequent fast attachment of new buiding blocks. Depending on $\Delta\mu$, the relative growth rates of 19° Ga and 19° Se edges also change. Since the growth rate of a Ga-zigzag edge is much higher than that of a Se-zigzag edge at $\Delta\mu$ = 0.06 eV, the circular nucleus first grows into a truncated triangle with its long and short edges being Se-zigzag and Ga-zigzag edges (Figure 5d). Further growth would transform the truncated triangle into a triangle enclosed by only Se-zigzag edges. In contrast, the circular nucleus would evolve into a triangle with only Ga-zigzag edges at $\Delta\mu$ = 0.24 eV because of the lower growth rate of Ga-zigzag edges compared to Se-zigzag edges (Figure 5f). In addition, by varying $\Delta\mu$ from 0.06 to 0.24 eV, GaSe flakes are also predicted to grow into shapes ranging from truncated triangles to hexagons enclosed by alternative Se- and Ga-zigzag edges (Figure S9a−f). The theoretical modeling based on KWC theory is reasonably consistent with the experimental results, in which the as-grown monolayer GaSe flakes generally show triangular (with minor truncated triangular) shapes with zigzag edges. From these observed shapes, it is deduced that the real $\Delta\mu$ in our experiment may be on either side of 0.15 eV (the cross point of Ga- and Se-zigzag in Figure 5b), very close to either 0.06 or 0.24 eV. More importantly, the experimental results and theoretical modeling indicate that morphology control on the monolayer flakes is possible by adjusting $\Delta\mu$ in the synthesis.

In addition to the growth kinetics, we also modeled the shape evolution of GaSe flakes and etched holes during etching. Under idealized conditions, where etching is only governed by atom detachment from edges, the external contour evolution follows a process that is inverse to that predicted by the KWC theory, that is, edges with locally fastest etching rate should appear and dominate the perimeter. Figure 5g,h shows the simulated etching process of an as-grown GaSe flakes with the etching rate profiles the same as those for grown ones at $\Delta\mu$ = 0.06 (with Se-zigzag edges) and 0.24 eV (with Ga-zigzag), respectively. The two cases show similar etching patterns. At the initial stage of the etching from the outside edges, the fast etching 19° edges (with respect to the Se- or Ga-zigzag edges) generally appear first at the vertices of the as-grown triangular GaSe flakes because they are less stable than the edges. Further etching leads to the fast shortening of zigzag Se (Ga) edges and transformation of the triangular external contour into a dodecagon with only 19° edges (Figure 5g,h). However, in the experiment most of the etched monolayer triangular flakes keep a similar contour as before etching (see Figures 1 and 2), while some are found to be etched into a polygon mainly showing tilt edges with a tilt angle about 9° with respect to the zigzag Se (Ga) edge, as shown in Figure 5i. Such an inconsistency between the theoretical model and experimental results is possibly due to the interaction between the GaSe monolayer and SiO_2/Si substrate, and the effect of defects on etching, which were not included in the modeling. However, we did observe that the second triangular layers of the as-grown bilayer GaSe flakes with sharp vertices (Figure 5j) exhibit new edges at the vertices after etching (Figure 5k,l). The angle of the two newly formed edges with respect to the zigzag Se (Ga) edge is about 18° (Figure 5l), very close to the predicted 19° edges. This corresponds well with the theoretical models on the initial etching stage. Given the fact that the interlayer interaction of bilayer GaSe is different from the interaction between GaSe and amorphous SiO_2, it suggests that the

substrate can greatly affect the etching process, which will be studied in detail in the future. In addition to the etching of outer edges, our models also simulated the shape evolution of etched holes (Figure 5g,h). As shown by the models, the hole morphology changes from hexagons or truncated triangles to triangles with their orientation opposite to (i.e., rotated by 60°) as-grown triangles to ensure that they have the same types of edges, and the flakes would be eventually etched into three small pieces. Such a hole morphology evolution predicted by KWC has not been directly observed experimentally. For example, as shown in Figure 2a−f, the etched holes at different etching stages are all triangles, although the KWC-simulated morphologies such as hexagons and truncated triangles are indeed observed at the early stage of etching from the experimental results (Figure 1e−i). The inconsistency could also be attributed to the interactions between the substrate and GaSe monolayers or due to the small particles in the center that could influence the initial shape of the etched hole. Despite the initial shape of the etched hole, the hole finally evolves into the most stable one as modeled by KWC. It is worth noting that the edge and shape evolution of the etched holes during etching (Figure 5g,h) is the same as that of the flakes during growth (Figure 5d,f), but such a shape evolution was rarely observed experimentally in the growth, which could be due to a much faster rate of growth than that of etching. This further demonstrates that studying the etching process can shed light on the growth mechanism of 2D crystals.

Finally, we investigated the etching of grain boundaries formed by merging two single-crystalline GaSe monolayers, which lead to irregularly shaped domains. As already shown above, the grain boundaries are energy-favorable for the formation of etched holes. At the initial etching stage, small, separated holes are formed on the boundary and start to propagate into each crystal (Figure 6a,b). It is interesting to note that the etching pattern on each crystal from the boundary also follows the shape of an equilateral triangle, truncated triangle, or hexagon in a direction opposite to the triangular crystal (Figure 6c−f). Therefore, the morphology of the etched hole on the boundary varies depending on the orientation of the two triangular monolayers that merged (Figure 6c−f).

■ CONCLUSIONS

In conclusion, the growth, etching, and regrowth processes of monolayer GaSe crystals (including single-crystalline triangles and irregular-shaped domains formed by merged triangles) were studied by altering the vapor delivery and chemical potential of reactants by tuning the argon carrier gas. Etching of monolayers occurs not only from the edges, but also from the centers, creating etched holes. The morphology evolution of the monolayer GaSe crystals and etched holes during the growth and etching processes was found to be edge-structure-dependent and follow KWC theory, and could be modeled theoretically at the atomic level through the different formation energies of nucleus/dents for different types of edges (i.e., zigzag, armchair, and slanted) moderated by the chemical potential difference $\Delta\mu$ between Ga and Se. This model explains the experimental results that the as-grown monolayer GaSe flakes generally show triangular (with minor truncated triangular) shapes with zigzag edges, as well as the observation that the etched hole morphology changes from hexagons or truncated triangles to triangles with their orientation rotated by 60° relative to the parent flakes. Our study provides some insight into the growth kinetics of 2D binary crystals, which is
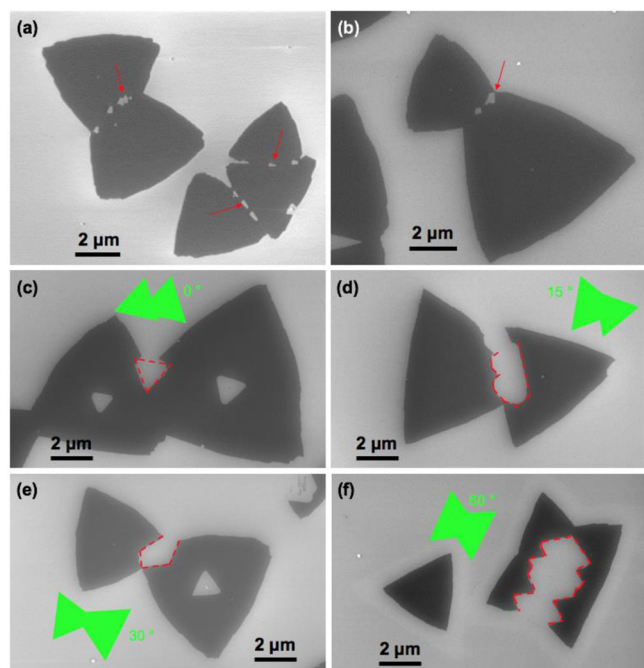
Figure 6. Etching on the grain boundaries. (a, b) SEM images of monolayer GaSe domains formed by merging triangular crystals after being etched for 1 min. The red arrows indicate that the etched holes start to form at the boundaries. (c–f) SEM images showing the shape evolution of the etched holes formed at the boundaries of two merged triangular GaSe monolayers at different orientations after etching for 5 min.

helpful for further understanding the growth mechanisms of 2D materials. More importantly, the theoretical simulation predicts the possibility of tailoring the morphology and growing much larger-sized, single-crystalline GaSe monolayers with higher crystal quality through the precise tuning of chemical potentials and optimization of conditions in the growth–etching–regrowth process. Based on these principles, after creating etched holes in GaSe monolayers, introducing other source materials in the regrowth process can be envisioned to fill the hole and tailor the crystal shapes to reliably produce new families of novel core–shell 2D lateral heterostructures.

■ EXPERIMENTAL SECTION

Materials Synthesis and Etching. The synthesis of 2D GaSe was carried out in a tube furnace system equipped with a 1 in. quartz tube. Bulk GaSe (synthesized as described in our previous work) and Ga_2Se_3 (99.99%, Alfa Aesar) crystals were mixed together ($GaSe/Ga_2Se_3$ molar ratio ~50:1) and were used as source materials. SiO_2 (~300 nm)/Si pieces (1×1 cm^2) were cleaned with acetone, isopropyl alcohol (IPA), and DI water, and used as growth substrates. In a typical run, ~60 mg of source powder and a piece of SiO_2/Si substrate were loaded on a quartz boat and subsequently inserted into the furnace. The source was located at the center of the furnace, with the substrate located ~8–10 cm downstream. After evacuating the tube to ~5×10^{-3} Torr, the reaction was conducted at 750 °C (with a ramping rate of 20 °C/min) for 3 min at a pressure of 30 Torr and an argon carrier gas flow rate of 60 sccm. The vapor-phase reactants were transported by the flowing argon gas to the growth region, in which the temperature was ~710–720 °C, thereby feeding the growth of the 2D GaSe crystals. After growth, the furnace was cooled naturally to room temperature. The etching was conducted during the growth by cutting off the argon carrier gas, stopping pumping (closing the throttle valve connected to the pump), and immediately increasing the

furnace temperature to 760 °C. During the etching process, the pressure in the reaction tube remained unchanged.

Characterization Methods. The morphologies of the as-grown 2D GaSe crystals and etched monolayers were characterized using optical microscopy (Leica DM4500 P), SEM (Zeiss Merlin SEM), and AFM (Bruker Dimension Icon AFM). The crystal structures of the as-grown and etched GaSe monolayers were investigated using an aberration-corrected Nion UltraSTEM operating at 100 kV, using a half-angle range of the ADF detector from 86 to 200 mrad. The samples for STEM analysis were grown directly on amorphous silicon films (5 nm in thickness) supported by silicon TEM grid using the same growth process as described above.

Theoretical Calculations. DFT calculations are carried out by using the Vienna ab initio Simulation Package (VASP).[39,40] Projected augmented wave (PAW) method is used to describe the interaction between valence electrons and ion cores.[41] Generalized gradient approximation (GGA) for the exchange-correlation energy is employed, since it performs well on calculating covalent bonds.[42] The energy cutoff for the plane wave basis is 400 eV. All the structures are fully optimized until the energy and force converge to 1×10^{-4} eV and 0.02 eV/Å, respectively. For the calculation of GaSe nanoribbons and flakes, Monkhorst–Pack k-point mesh is sampled with $5 \times 1 \times 1$ and $1 \times 1 \times 1$, respectively.[43] A vacuum layer of at least 1.2 nm thick is used in the unitcells of these structures to avoid periodic image interaction.

Due to the 3-fold symmetry of hexagonal GaSe, it is impossible to obtain the respective edge formation energies of Ga- and Se-terminated zigzag edges through a ribbon structure. However, this can be realized through calculating the energies of triangular GaSe flakes with only Ga- or Se-terminated edges (as shown in Figure S6). To differentiate Ga and Se, their energies are defined as $(\varepsilon_{GaSe})/2 \pm \Delta\mu$ eV, with the energy of a GaSe dimer, ε_{GaSe}, in a hexagonal GaSe monolayer calculated to be −7.60 eV. For example, the formation energy (γ_{Ga}) of a Ga-terminated zigzag edge can be obtained by differentiating the energies of two different triangular flakes with Ga-terminated zigzag edges, whose total energy is $N_{Ga} \times \mu_{Ga} + N_{Se} \times \mu_{Se} + 3 \times l \times \gamma_{Ga} + 3 \times \nu$, where N_{Ga} and N_{Se} are the number of Ga and Se atoms, μ_{Ga} and μ_{Se} are the energies of Ga and Se atoms, and ν is the energy of the vertex of the triangle structure. The armchair, Se-terminated zigzag, and Ga-terminated zigzag edge formation energies are 3.06 eV/nm, $1.47 + 1.75 \times \Delta\mu$ eV/nm, and $2.91 + 3.49 \times \Delta\mu$ eV/nm. With these data, the edge formation energy profiles at different $\Delta\mu$ as a function of edge tilt angle can be obtained, which are shown in Figure S7b.

To obtain the formation energy profiles of the growth of different edges, the step flow growth model is employed, and the formation energies of attaching atoms to the edges step by step are calculated, as shown in Figure S8. The formation energy change, E_F, is defined as

$$E_F = E_i - E_{ref} - N_{Ga}\mu_{Ga} - N_{Se}\mu_{Se}$$

where E_i is the energy of the ith edge strcture with N_{Ga} Ga and N_{Se} Se atoms attached to the reference edge structure for growth; E_{ref} is the energy of the reference structure; and μ_{Ga} and μ_{Se} are energies of Ga and Se atoms.

The growth/etching rate of an edge with an arbitrary tilt angle with respect to the zigzag edge can be approximated simply as

$$R(\theta) \approx C_{ZZ}(\theta) \times \exp(-E^*_{F\text{-}ZZ}/k_BT) + C_{AC}(\theta) \times \exp(-E^*_{F\text{-}AC}/k_BT) + C_K(\theta) \quad (1)$$

where C_{ZZ}, C_{AC}, and C_K are the concentrations of zigzag, armchair, and kink sites, respectively, and $E^*_{F\text{-}ZZ}$ and $E^*_{F\text{-}AC}$ are the formation energies for activating the growth of zigzag and armchair edges, respectively.[24,26,38] In particular, the growth rate of zigzag edge $R(0°)$ is estimated as

$$R(0) \approx (\exp(-E^*_{F\text{-}ZZ}/2k_BT) + \exp(-E^*_{F\text{-}ZZ}/k_BT))/a \quad (2)$$

Similarly, the growth rate of armchair edge $R(30°)$ is

$$R(\pi/6) \approx \frac{(\exp(-E^*_{\text{F-AC}}/2k_BT) + \exp(-E^*_{\text{F-AC}}/k_BT))}{(\sqrt{3})a} \qquad (3)$$

where a is the lattice constant of the hexagonal GaSe. The meaning of these two equations is straightforward. The first term comes from the propagation of the preformed zigzag (armchair) kinks, which is much higher than the second term resulting from forming new zigzag (armchair) kinks. The growth rate profiles at different $\Delta\mu$ is estimated from the calculated E^*_F, which is the highest formation energy during the growth process of zigzag or armchair edges (Figure S8). Taking $\Delta\mu = 0.06$ eV as an example, the growth rate ratio of $R_{\text{ZZSe}}/R_{\text{ZZGa}}/R_{\text{AC}}$ is roughly estimated to be 1:3:9 by eqs 2 and 3. Since 19° edges show locally the highest growth rates, we assume that $R_{\text{19-Se/19-Ga}} \approx 1.2 \times (R_{\text{ZZSe/ZZGa}} + R_{\text{AC}})$. This assumption is reasonable for kinetic Wulff construction simulation because the exact values of $R_{\text{19-Se/19-Ga}}$ would not change the shape evolution process qualitatively. The growth rate of other tilt edges is determined by linear interpolation between the local extrema determined above. Other growth rate profiles are also determined in the same way. The polar plots of these growth/etching rate profiles are shown in Figure S9. The growth rate profiles are also used to simulate the etching process. We note that the etching rate profile has the same form as that of growth rate profile. Furthermore, in our experiments, the growth and etching are carried out under near-equilibrium conditions; therefore, the growth and etching rates would have very similar values. The corresponding simulated growth and etching processes are also shown in Figure S8.

■ ASSOCIATED CONTENT

Ⓢ Supporting Information

The Supporting Information is available free of charge on the ACS Publications website at DOI: 10.1021/jacs.6b11076.

> AFM and SEM images, edge energy calculation models, formation energies, energy evolution flow diagram, and polar plots of the growth/etching rate profiles (PDF)

■ AUTHOR INFORMATION

Corresponding Authors

*E-mail: fding@ibs.re.kr.
*E-mail: xiaok@ornl.gov.

ORCID Ⓞ

Kai Xiao: 0000-0002-0402-8276

Author Contributions

X.L. and J.D. contributed equally to this work.

Notes

The authors declare no competing financial interest.

■ REFERENCES

(1) Geim, A. K.; Novoselov, K. S. *Nat. Mater.* **2007**, *6*, 183.

(2) Butler, S. Z.; Hollen, S. M.; Cao, L. Y.; Cui, Y.; Gupta, J. A.; Gutiérrez, H. R.; Heinz, T. F.; Hong, S. S.; Huang, J. X.; Ismach, A. F.; Johnston-Halperin, E.; Kuno, M.; Plashnitsa, V. V.; Robinson, R. D.; Ruoff, R. S.; Salahuddin, S.; Shan, J.; Shi, L.; Spencer, M. G.; Terrones, M.; Windl, W.; Goldberger, J. E. *ACS Nano* **2013**, *7*, 2898.

(3) Lopez-Sanchez, O.; Lembke, D.; Kayci, M.; Radenovic, A.; Kis, A. *Nat. Nanotechnol.* **2013**, *8*, 497.

(4) Wu, S.; Buckley, S.; Schaibley, J. R.; Feng, L.; Yan, J.; Mandrus, D. G.; Hatami, F.; Yao, W.; Vučković, J.; Majumdar, A.; Xu, X. *Nature* **2015**, *520*, 69.

(5) Kang, K.; Xie, S.; Huang, L.; Han, Y.; Huang, P. Y.; Mak, K. F.; Kim, C.-J.; Muller, D.; Park, J. *Nature* **2015**, *520*, 656.

(6) Ma, T.; Ren, W.; Liu, Z.; Huang, L.; Ma, L.-P.; Ma, X.; Zhang, Z.; Peng, L.-M.; Cheng, H.-M. *ACS Nano* **2014**, *8*, 12806.

(7) Li, X.; Cai, W.; An, J.; Kim, S.; Nah, J.; Yang, D.; Piner, R.; Velamakanni, A.; Jung, I.; Tutuc, E.; Banerjee, S. K.; Colombo, L.; Ruoff, R. S. *Science* **2009**, *324*, 1312.

(8) van der Zande, A. M.; Huang, P. Y.; Chenet, D. A.; Berkelbach, T. C.; You, Y.; Lee, G.-H.; Heinz, T. F.; Reichman, D. R.; Muller, D. A.; Hone, J. C. *Nat. Mater.* **2013**, *12*, 554.

(9) Wang, X.; Gong, Y.; Shi, G.; Chow, W. L.; Keyshar, K.; Ye, G.; Vajtai, R.; Lou, J.; Liu, Z.; Ringe, E.; Tay, B. K.; Ajayan, P. M. *ACS Nano* **2014**, *8*, 5125.

(10) Huang, J.-K.; Pu, J.; Hsu, C.-L.; Chiu, M.-H.; Juang, Z.-Y.; Chang, Y.-H.; Chang, W.-H.; Iwasa, Y.; Takenobu, T.; Li, L.-J. *ACS Nano* **2014**, *8*, 923.

(11) Li, X.; Lin, M.-W.; Puretzky, A. A.; Idrobo, J. C.; Ma, C.; Chi, M.; Yoon, M.; Rouleau, C. M.; Kravchenko, I. I.; Geohegan, D. B.; Xiao, K. *Sci. Rep.* **2014**, *4*, 5497.

(12) Schwierz, F. *Nat. Nanotechnol.* **2010**, *5*, 487.

(13) Radisavljevic, B.; Radenovic, A.; Brivio, J.; Giacometti, V.; Kis, A. *Nat. Nanotechnol.* **2011**, *6*, 147.

(14) Oura, K.; Lifshits, V. G.; Saranin, A. A.; Zotov, A. V.; Katayama, M. *Surface Science: An Introduction*; Springer: Berlin, 2003.

(15) Eaglesham, D. J.; Cerullo, M. *Phys. Rev. Lett.* **1990**, *64*, 1943.

(16) Li, X.; Basile, L.; Huang, B.; Ma, C.; Lee, J.; Vlassiouk, I. V.; Puretzky, A. A.; Lin, M.-W.; Yoon, M.; Chi, M.; Idrobo, J. C.; Rouleau, C. M.; Sumpter, B. G.; Geohegan, D. B.; Xiao, K. *ACS Nano* **2015**, *9*, 8078.

(17) Lin, Y.-C.; Lu, N.; Perea-Lopez, N.; Li, J.; Lin, Z.; Peng, X.; Lee, C. H.; Sun, C.; Calderin, L.; Browning, P. N.; Bresnehan, M. S.; Kim, M. J.; Mayer, T. S.; Terrones, M.; Robinson, J. A. *ACS Nano* **2014**, *8*, 3715.

(18) Azizi, A.; Eichfeld, S.; Geschwind, G.; Zhang, K.; Jiang, B.; Mukherjee, D.; Hossain, L.; Piasecki, A. F.; Kabius, B.; Robinson, J. A.; Alem, N. *ACS Nano* **2015**, *9*, 4882.

(19) Gong, Y.; Ye, G.; Lei, S.; Shi, G.; He, Y.; Lin, J.; Zhang, X.; Vajtai, R.; Pantelides, S. T.; Zhou, W.; Li, B.; Ajayan, P. M. *Adv. Funct. Mater.* **2016**, *26*, 2009.

(20) Geng, D.; Wu, B.; Guo, Y.; Luo, B.; Xue, Y.; Chen, J.; Yu, G.; Liu, Y. *J. Am. Chem. Soc.* **2013**, *135*, 6431.

(21) Guo, W.; Wu, B.; Li, Y.; Wang, L.; Chen, J.; Chen, B.; Zhang, Z.; Peng, L.; Wang, S.; Liu, Y. *ACS Nano* **2015**, *9*, 5792.

(22) Wang, L.; Wu, B.; Jiang, L.; Chen, J.; Li, Y.; Guo, W.; Hu, P.; Liu, Y. *Adv. Mater.* **2015**, *27*, 4858.

(23) Liu, Y.; Dobrinsky, A.; Yakobson, B. I. *Phys. Rev. Lett.* **2010**, *105*, 235502.

(24) Artyukhov, V. I.; Liu, Y.; Yakobson, B. I. *Proc. Natl. Acad. Sci. U. S. A.* **2012**, *109*, 15136.

(25) Shu, H.; Chen, X.; Tao, X.; Ding, F. *ACS Nano* **2012**, *6*, 3243.

(26) Ma, T.; Ren, W.; Zhang, X.; Liu, Z.; Gao, Y.; Yin, L.-C.; Ma, X.-L.; Ding, F.; Cheng, H.-M. *Proc. Natl. Acad. Sci. U. S. A.* **2013**, *110*, 20386.

(27) Zhang, Z.; Liu, Y.; Yang, Y.; Yakobson, B. I. *Nano Lett.* **2016**, *16*, 1398.

(28) Cao, D.; Shen, T.; Liang, P.; Chen, X.; Shu, H. *J. Phys. Chem. C* **2015**, *119*, 4294.

(29) Hu, P. A.; Wen, Z. Z.; Wang, L. F.; Tan, P. H.; Xiao, K. *ACS Nano* **2012**, *6*, 5988.

(30) Lei, S.; Ge, L.; Liu, Z.; Najmaei, S.; Shi, G.; You, G.; Lou, J.; Vajtai, R.; Ajayan, P. M. *Nano Lett.* **2013**, *13*, 2777.

(31) Zhou, Y.; Nie, Y.; Liu, Y.; Yan, K.; Hong, J.; Jin, C.; Zhou, Y.; Yin, J.; Liu, Z.; Peng, H. *ACS Nano* **2014**, *8*, 1485.

(32) Zhou, X.; Cheng, J.; Zhou, Y.; Cao, T.; Hong, H.; Liao, Z.; Wu, S.; Peng, H.; Liu, K.; Yu, D. *J. Am. Chem. Soc.* **2015**, *137*, 7994.

(33) Cao, T.; Li, Z.; Louie, S. G. *Phys. Rev. Lett.* **2015**, *114*, 236602.

(34) Li, X.; Lin, M.-W.; Lin, J.; Huang, B.; Puretzky, A. A.; Ma, C.; Wang, K.; Zhou, W.; Pantelides, S. T.; Chi, M.; Kravchenko, I.; Fowlkes, J.; Rouleau, C. M.; Geohegan, D. B.; Xiao, K. *Sci. Adv.* **2016**, *2*, e1501882.

(35) Rudolph, R.; Pettenkofer, C.; Bostwick, A. A.; Adams, J. A.; Ohuchi, F.; Olmstead, M. A.; Jaeckel, B.; Klein, A.; Jaegermann, W. *New J. Phys.* **2005**, *7*, 108.

(36) Bollinger, M. V.; Jacobsen, K. W.; Nørskov, J. K. *Phys. Rev. B: Condens. Matter Mater. Phys.* **2003**, *67*, 085410.

(37) Bollinger, M. V.; Lauritsen, J. V.; Jacobsen, K. W.; Nørskov, J. K.; Helveg, S.; Besenbacher, F. *Phys. Rev. Lett.* **2001**, *87*, 196803.

(38) Ding, F.; Harutyunyan, A. R.; Yakobson, B. I. *Proc. Natl. Acad. Sci. U. S. A.* **2009**, *106*, 2506.

(39) Kresse, G.; Hafner, J. *Phys. Rev. B: Condens. Matter Mater. Phys.* **1993**, *48*, 13115.

(40) Kresse, G.; Furthmüller, J. *Comput. Mater. Sci.* **1996**, *6*, 15.

(41) Kresse, G.; Joubert, D. *Phys. Rev. B: Condens. Matter Mater. Phys.* **1999**, *59*, 1758.

(42) Perdew, J. P.; Burke, K.; Ernzerhof, M. *Phys. Rev. Lett.* **1996**, *77*, 3865.

(43) Monkhorst, H.; Pack, J. *Phys. Rev. B* **1976**, *13*, 5188.